

Numerical simulation of free cross-shaped jet

A. Meslem*, A. Dia*, C. Beghein*, A. Ammar*, I. Nastase**, M. El Hassan*

*LEPTIAB, Université de La Rochelle, Pôle Sciences et Technologie, La Rochelle, France, E-mail: ameslem@univ-lr.fr

**CAMBI, Technical University of Civil Engineering, Bucharest, Romania, E-mail: ilinca.nastase@cambi.ro

crossref <http://dx.doi.org/10.5755/j01.mech.18.4.2328>

1. Introduction

The lobed nozzles are commonly used under very high Reynolds number in aeronautics and combustion applications for thrust improvement and noise reduction [1-3]. Under low or moderate Reynolds numbers for HVAC applications, the analysis of lobed nozzle and orifice jets shows that large streamwise structures generated by the lip of the lobed diffuser are present and control the ambient air induction [4-7]. The previous experimental studies provided some knowledge on the physical phenomena at the origin of their particular performance. An innovative concept for optimized air diffusion in buildings using passive control of air jet through lobed diffusers was also proposed [8, 9]. This concept reposes on the idea of relatively costless and simple modifications of the exit boundary geometry of classical existing diffusers. At each elementary cross-shaped orifice of a perforated panel diffuser, large scale structures develop in the orifice troughs and control air induction in the jet near field [4, 9]. The perforated panel flow induction depends heavily on elementary orifice geometry parameters and designing optimal orifice geometry by experimental means alone is quite expensive due to the wide range of parameters involved. Computational Fluid Dynamics (CFD) based methods represents a better alternative to experimental methods in the case of optimization studies. Reynolds-Averaged Navier-Stokes (RANS) equation solvers were used routinely for the analysis of aeronautic and aerospace systems. Passive controlled engine exhaust nozzles were numerically analyzed at high exit Reynolds number in terms of their performance quantities and noise reduction [10-15]. RANS models replace all turbulent fluid dynamic effects with a turbulence model. When they have been successful in calculating thrust, noise prediction is not as satisfactory. In fact, despite significant work to improve RANS-based methods they seem to have limitations to accurately predict the turbulent fluid structures that cause jet noise and mixing in high Reynolds number flows with significant three-dimensionality [13]. For six lobed circular nozzle at exit Reynolds number of 5.5×10^4 , Nathan et al. [15] found that numerical simulations using four widely employed turbulence models - among them Shear-Stress Transport (SST) $k\omega$ turbulence model - agree reasonably well with the Particle Image Velocimetry (PIV) measurements in terms of streamwise vorticity and spanwise vorticity. However, the turbulent kinetic energy is over predicted.

In our case, the Reynolds number is lower and the diffuser geometry optimization is based on the mean flow characteristics such as jet volumetric flow rate and jet expansion.

In this study the flow dynamics of isothermal, turbulent cross-shaped free jet is investigated both numeri-

cally and experimentally. Numerical and experimental results are compared to assess the capability and limits of the turbulence model SST $k\omega$ to provide near field orifice lobed jet characteristics at moderate Reynolds number.

2. Experimental campaign

The air jet is generated using a cross-shaped orifice (Fig. 1). The equivalent diameter based on the orifice exit area is $D_e = 10$ mm. The air blowing facility consists of an axial miniature fan placed inside one meter long metallic pipe of 0.16 m diameter. A convergent duct placed at the end of the pipe ensures the reduction of the turbulence level at the jet exit. A honeycomb structure is positioned just upstream of the convergent duct. The initial Reynolds number based on the maximum exit velocity and on the equivalent diameter D_e is around 4000 (Table 1).

Table 1

Method	Exit conditions				
	Q_0 , m ³ /s	U_{0mean} , m/s	U_{0m} , m/s	$U_{0mean}D_e/\nu$	$U_{0m}D_e/\nu$
PIV	3.47×10^{-4}	4.42	6.41	2815	4063
SST $k\omega$ Model	3.06×10^{-4}	3.90	5.36	2484	3414

0: initial *m*: maximum

Two-dimensional Dantec PIV is used to measure longitudinal distribution of flow streamwise velocity in the Major Plane (MP) and minor Plane (mP) defined in Fig. 1. The system is made up of a 200 mJ dual Yag laser, a synchronizer, a high-sensitivity CCD camera of 4000×2672 pix² resolution and the Dynamic Studio software for data acquisition, processing and post processing. The lasers emit 532 nm wavelength pulse light, the thickness of the light sheet is about 1 mm. The acquisition frequency of the PIV system is 1 Hz and a total of 500 image couples were acquired. The jet was seeded with small olive oil droplets, 1 to 2 μ m in diameter, provided by a liquid seeding generator. It is assumed that tracer particle sliding is negligible. The calibrated image gives a spatial resolution of 40.6 μ m per pixel which corresponds to a 162.3×108 mm² field of view. Images are processed through an adaptive multigrid correlation algorithm handling the window distortion and the sub-pixel window displacement. The prediction-correction method is validated for each grid size when the signal to noise ratio of the correlation is above a threshold of 1.1. In average, less than 1% of the vectors are detected as incorrect. These incorrect vectors are corrected by using a bilinear interpolation scheme. The final size of the interrogation windows gives a spatial resolution of 0.49 mm.

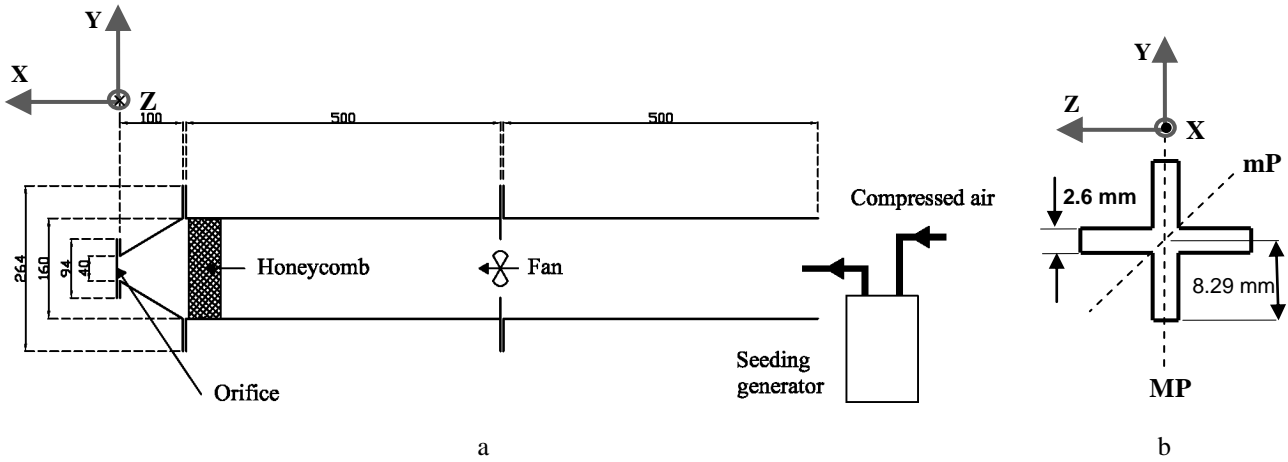


Fig. 1 Exit conditions: (a) air jet facility sketch (b), orifice's geometry (b)

The obtained velocity field is extended from the jet exit to $X = 15.5D_e$ in the longitudinal direction. The obtained mean streamwise velocity field is shown in Figs. 3 (1a) and (1b) using isovalues (color map) representation.

The velocity fields in transverse planes (YZ) at different axial positions $0.5D_e \leq X \leq 5D_e$ are obtained using time-resolved stereoscopic PIV measurements (the mean streamwise velocity contours are plotted in Fig. 5). The PIV system is composed of two Phantom V9 cameras of 1200×1632 pixels² and a Nd: YLF NewWave Pegasus laser of 10 mJ energy and 527 nm wavelength. The acquisition frequency of the PIV system is 500 Hz for a maximal image window. In each plane, a number of 1000 image couples were acquired. The two cameras are mounted on a traversing system with an angle of 45° to the normal position of the light sheet plane of the laser. The lenses are separated from the camera in order to shift the CCD-chip plane with respect to the lens plane, in the way that the Scheimpflug conditions are satisfied. The calibrated image gives a spatial resolution of $60 \mu\text{m}$ per pixel which corresponds to a $98 \times 72 \text{ mm}^2$ field of view. Images are processed through an adaptive multi-grid correlation algorithm handling the window distortion and the sub-pixel window displacement. The prediction-correction method is validated for each grid size when the signal to noise ratio of the correlation is above a threshold of 1.1. In average, less than 3% of the vectors are detected as incorrect. The final grid is composed of 16×16 pixels² size interrogation windows with 50% overlapping leading to a spatial resolution of 0.39 mm. The same liquid seeding generator as for the classical PIV measurements was used. More details about the time-resolved stereoscopic PIV technique are given by [7].

3. Computational details

The flow considered in this study is weakly turbulent, and a turbulent model is thus required for the computation of the flow. Of the various models that are available, the widely used RANS Shear Stress Transport (SST) $k\omega$ turbulence model [16] has been chosen.

The computational domain (Fig. 2, a) is composed of two parts separated by the orifice plate having 1.5 mm in thickness. The upstream part and the downstream part of the domain have the dimensions of $10 \times 10 \times 10D_e$ and $30 \times 10 \times 10D_e$ respectively. The inlet boundary conditions

for the simulation are given at the inlet plane of the upstream part of the domain. On this plane a uniform velocity of 0.00728 m/s and a turbulence intensity of 2% are specified. Owing to the symmetry of the problem, just one quarter of the flow is modeled. The other boundary conditions are mentioned in the Fig. 2.

The numerical analysis is performed using a finite volume based solver StarCCM+ Version 5.04. The SIMPLE algorithm is used for pressure-velocity coupling. The flow variables are calculated on a collocated grid. A second order upwind scheme is used to calculate the convective terms in the equations. A grid size of 1.4 million regular Cartesian nonuniform cells has been considered for the investigation. This grid is highly refined in the orifices plane (see Fig. 2, b). The values of y^+ for the first gridline off the surfaces of the plate are less than 4 which is acceptable for the low Reynolds number formulation of the considered model.

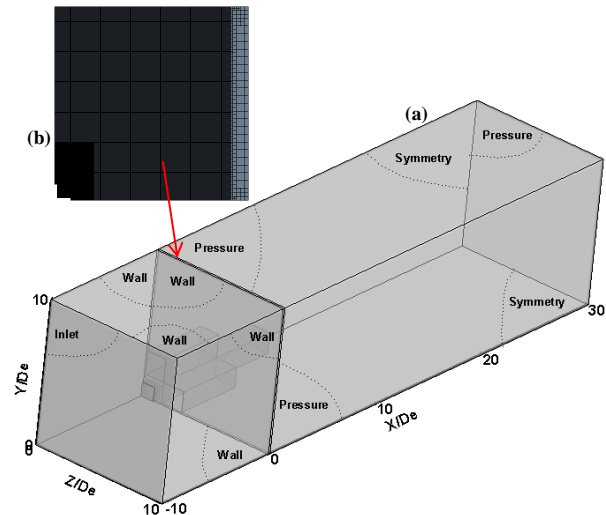


Fig. 2 (a) – 3D view of the domain; (b) – the surface mesh on the orifice plate

4. Results and discussion

The jet inlet conditions (i.e. flow characteristics at the orifice) are given in Table 1 for the measured flow and the simulated flow respectively. Mean characteristics of the initial boundary layers are given in Table 2. The values of the shape factor H for MP and mP suggest that the ini-

tial boundary layers are laminar in the two cases (real and simulated flows). However, the values of the initial momentum thickness (θ_0) and the initial displacement thickness (δ^*) in the real flow are greater than the ones obtained for the calculated flow.

Table 2

Initial boundary layer characteristics in the major and minor planes at $X = 0.1D_e$

Method	Boundary	δ^*/D_e	θ_0/D_e	$H=\delta^*/\theta_0$
PIV	MP	0.216	0.051	4.45
	mP	0.197	0.038	5.23
SST $k\omega$ Model	MP	0.100	0.027	3.67
	mP	0.053	0.014	3.38

MP: major plane; mP: minor plane; δ^* : displacement thickness; θ_0 : momentum thickness

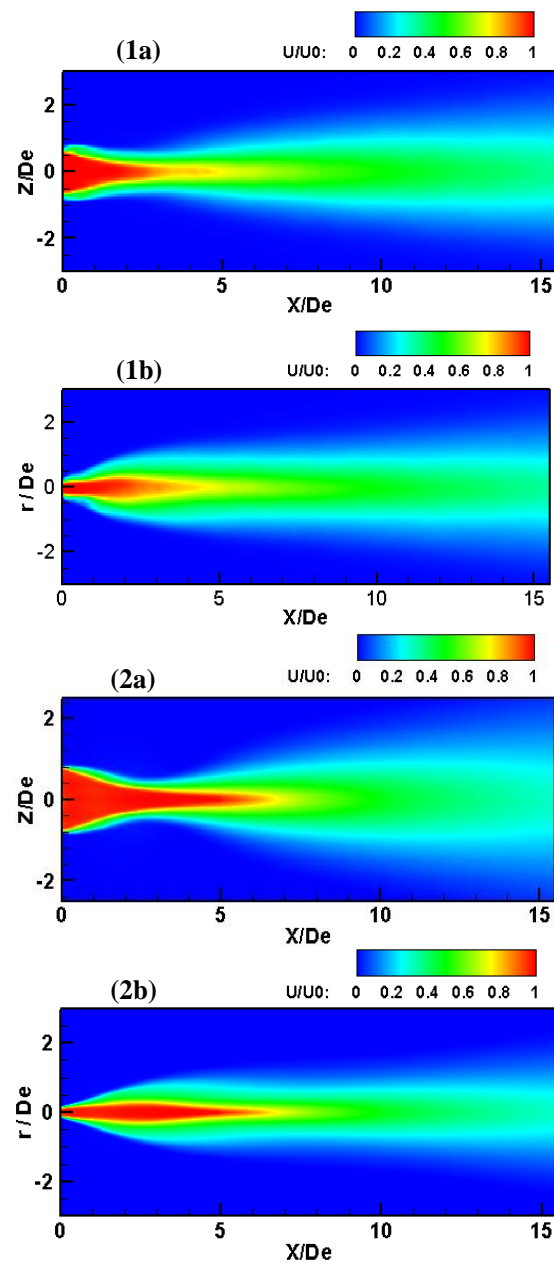


Fig. 3 Isocontours of the streamwise velocity in the symmetry plane (XZ): experiments (1); SST $k\omega$ Model (2); major plane (a); minor plane (b)

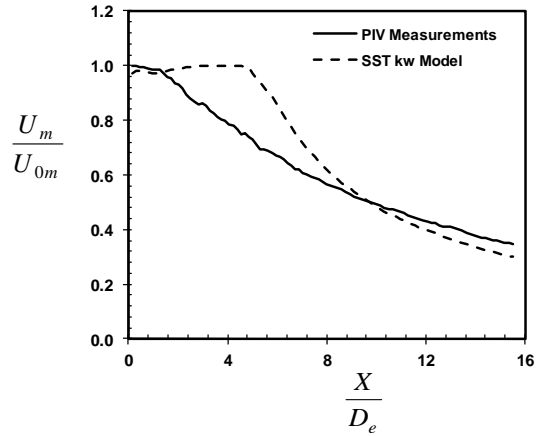


Fig. 4 Comparison of the streamwise velocity decay on jet centerline

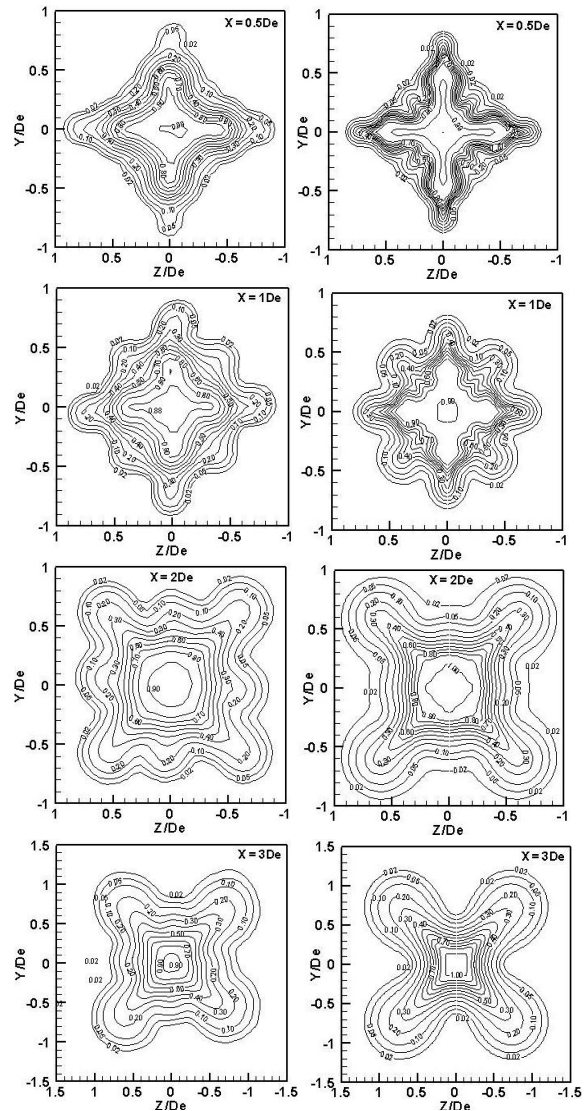


Fig. 5 Streamwise velocity contours in jet transverse planes: PIV measurements (left); Numerical simulation (right)

The MP and mP streamwise mean velocity isocontours given in Fig. 3, show that the global behaviour of the simulated flow is similar to the real one. Jet contraction in the MP and jet expansion in the mP, between $X = 0.5D_e$ and $X = 3D_e$, are due to the axis-switching phenomenon [4, 17]. However, the model overpredicts jet potential core length. Potential core length overestimation is also visible

on the streamwise maximum velocity evolution (Fig. 4). Acceptable predicted values are obtained beyond $X = 8D_e$ position.

In Fig. 5, streamwise velocity contours in the jet near field are given at different flow transverse planes. The axis-switching which occurs between $X = 0$ and $X = 3D_e$ is well predicted by the model with a slight lead in its prediction.

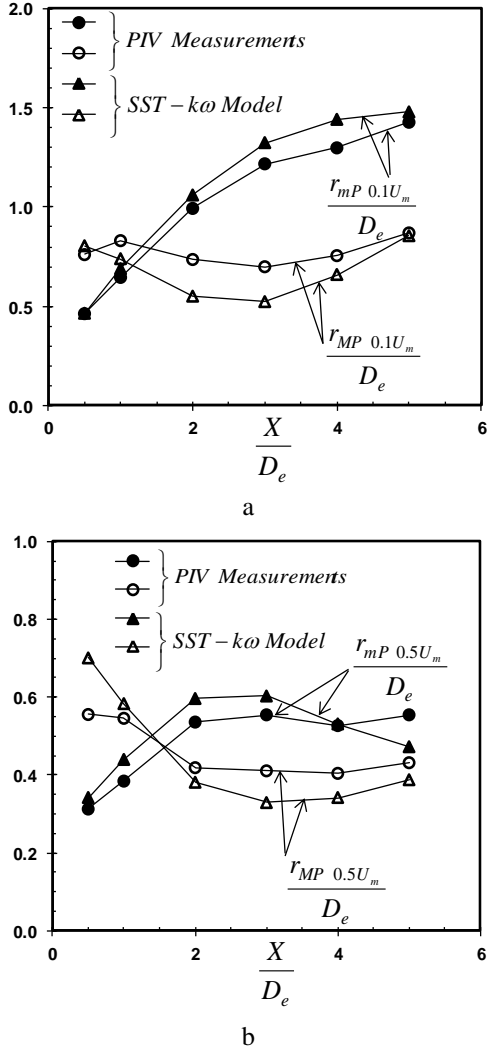


Fig. 6 Jet velocity widths comparison: (a) $0.1U_m$ - jet width; (b) $0.5U_m$ - jet width

Even if the model predicts the axis-switching phenomenon, the isocontours comparison reveals that the spatial distribution of the flow is not perfectly predicted by the model: the inner contours are tight and contraction/expansion in the MP/mP is more pronounced than in reality. In order to quantify the gap of the model prediction in the flow spatial distribution, we represent in Fig. 6 the jet thicknesses evolutions in the MP and the mP, given by $U = 0.5U_m$ and $U = 0.1U_m$ positions, where U_m is the maximum velocity at the considered streamwise position X . The flow spreading thicknesses $r_{0.5U_m}$ and $r_{0.1U_m}$ in the two planes, confirm the slight advance of the model in predicting the crossover phenomenon. These curves also confirm the pronounced character of axis-crossover. What is relevant however to note is the very good prediction of the average radius $r_{mean\ 0.1U_m} = \sqrt{S_{0.1U_m}/\pi}$ (Fig. 7) based on

the transverse flow area $S_{0.1U_m} = \int dS \Big|_{U>0.1U_m}$.

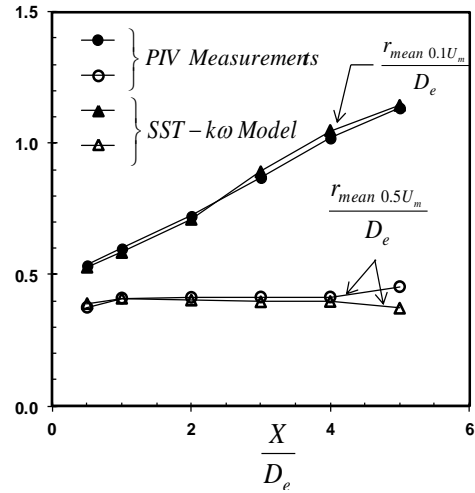


Fig. 7 Mean flow radii comparison

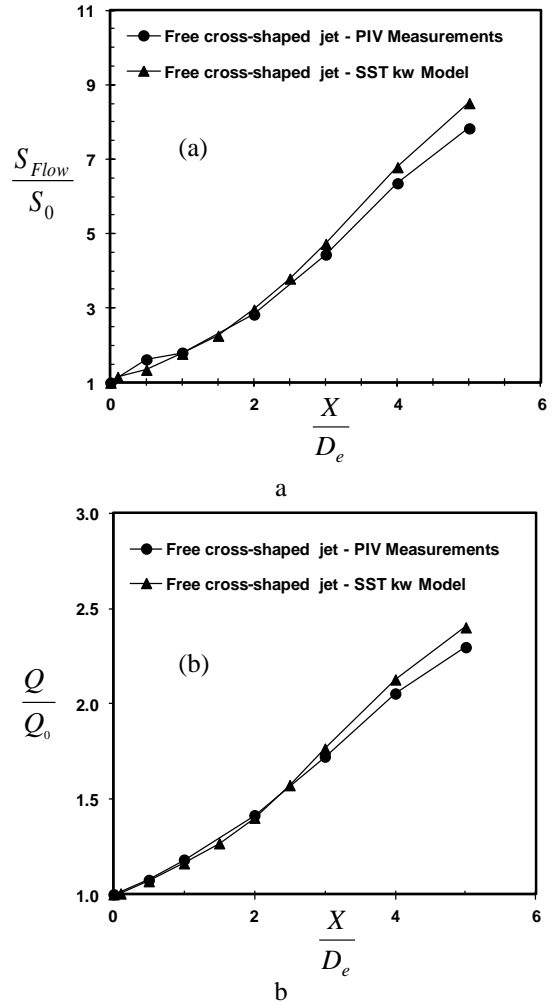


Fig. 8 (a) comparison of the streamwise evolutions of the jet flow area; (b) comparison of the streamwise evolutions of the jet volumetric flow rate

The average radius $r_{mean\ 0.5U_m} = \sqrt{S_{0.5U_m}/\pi}$ based on the transverse flow area $S_{0.5U_m} = \int dS \Big|_{U>0.5U_m}$ is less well predicted for $4D_e \leq X \leq 5D_e$. This suggests that the induction phenomenon is correctly reproduced by the

model, but mixing of the induced air and the jet air, is not perfectly reproduced. This explains the poor prediction of the decay of the axial velocity (Fig. 4). The tightening of the inner contours of the axial velocity observed previously (Fig. 5) is another consequence of the deficit model prediction of the mixing.

As expected, prediction of the volumetric flow rate defined in this study by $Q = \int U dS \Big|_{U>0.15m/s}$ is quite satisfactory (Fig. 8). The satisfactory comparison of the global jet expansion, given by jet flow area (Fig. 8, a), and the one of the jet volumetric flow rate (Fig. 8, b), suggest considering mean jet velocity, given by $U_{mean}(X) = Q(X) / S_{Flow}(X)$, where $S_{Flow} = \int dS \Big|_{U>0.15m/s}$ as a more reliable quantity of the model prediction of the jet streamwise velocity evolution (Fig. 9). As shown in Fig. 9, except for the first point at $X = 0.5D_e$, the mean jet velocity U_{mean} is well predicted by the model.

Evolutions of the integral of turbulence kinetic energy k along the X -axis from the numerical and the experimental transverse fields are given in Fig. 10. The turbulence kinetic energy increases with the axial distance for both experimental and simulated flows. However, as found by Nathan et al. [15], the SST $k\omega$ model overpredicts turbulent values.

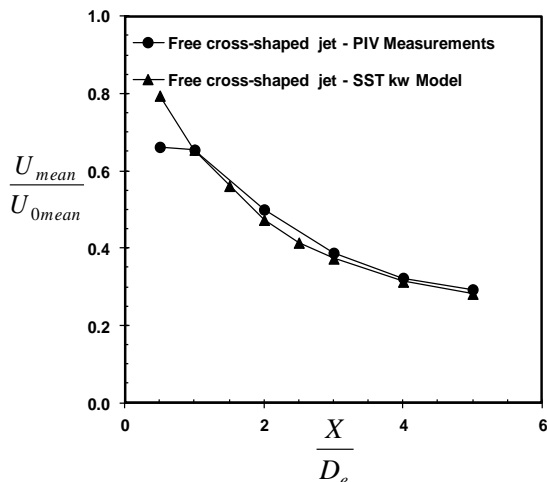


Fig. 9 Comparison of the streamwise evolutions of the jet mean velocity

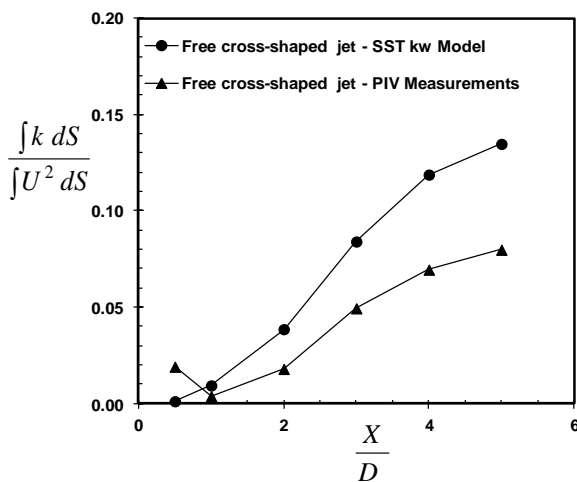


Fig. 10 Integral turbulent kinetic energy comparison

5. Conclusion

This study allowed assessing the capability and the limits of the turbulence model SST $k\omega$ to provide the orifice lobed flow characteristics at moderate Reynolds number. The numerical results are compared to experimental measurements. The axis-switching phenomenon of the jet which occurs between $X = 0$ and $X = 3D_e$ is well predicted by the model. Mean characteristics of the initial boundary layers are lower than reference values. Turbulent kinetic energy is over predicted. The flow expansion in the minor plane and flow contraction in the major plane are more pronounced and the potential core length is overestimated generating a delay on the streamwise maximum velocity decay. However, satisfactory predictions of the flow transverse area and its volumetric flow rate are observed and lead to good predictions of the streamwise evolutions of “mean flow radius” and “mean flow velocity”.

Consequently, the most notable conclusion of the present study is that the simulation approach using two-equation turbulence model SST $k\omega$ can successfully predict many significant features about the orifice lobed jet at moderate Reynolds number. The well predicted quantities will be used for designing optimal geometrical parameters of the lobed orifice for HVAC application.

References

1. **Hu, H.; Saga, T.; Kobayashi, T.; Taniguchi, N.** 2001. A study on a lobed jet mixing flow by using stereoscopic particle image velocimetry technique, *Physics of Fluids* 13(11): 3425-3441. <http://dx.doi.org/10.1063/1.1409537>.
2. **Gutmark, E.J.; Grinstein, F.F.** 1999. Flow control with noncircular jets, *Annual Reviews of Fluid Mechanics* 31: 239-272. <http://dx.doi.org/10.1146/annurev.fluid.31.1.239>.
3. **Belovich, V.M.; Samimy, M.** 1997. Mixing processes in a coaxial geometry with a central lobed mixer-nozzle, *AIAA Journal* 35(5): 838-841. <http://dx.doi.org/10.2514/2.7455>.
4. **Nastase, I.; Meslem, A.; Gervais, P.** 2008. Primary and secondary vortical structures contribution in the entrainment of low Reynolds number jet flows, *Experiments in Fluids* 44(6): 1027-1033. <http://dx.doi.org/10.1007/s00348-008-0488-2>.
5. **Nastase, I.; Meslem, A.** 2008. Vortex dynamics and entrainment mechanisms in low Reynolds orifice jets, *Journal of Visualisation* 11(4): 309-318. <http://dx.doi.org/10.1007/BF03182199>.
6. **Nastase, I.; Meslem, A.** 2010. Vortex dynamics and mass entrainment in turbulent lobed jets with and without lobe deflection angles, *Experiments in Fluids* 48(4): 693-714. <http://dx.doi.org/10.1007/s00348-009-0762-y>.
7. **El-Hassan, M.; Meslem, A.** 2010. Time-resolved stereoscopic PIV investigation of the entrainment in the near-field of circular and daisy-shaped orifice jets, *Physics of Fluids* 22(035107): 26p.
8. **Nastase, I.; Meslem, A.; Iordache, V.; Colda, I.** 2011. Lobed grilles for high mixing ventilation - An experimental analysis in a full scale model room, *Building and Environment* 46: 547-555. <http://dx.doi.org/10.1016/j.buildenv.2010.08.008>.

9. **Meslem, A.; Nastase, I.; Allard, F.** 2010. Passive mixing control for innovative air diffusion terminal devices for buildings, *Building and Environment* 45: 2679-2688.
<http://dx.doi.org/10.1016/j.buildenv.2010.05.028>.
10. **Hu, H.; Wu, S.S.** 1997. Computational studies of lobed forced mixer flows, *Journal of Thermal Science* 7(1): 22-28.
<http://dx.doi.org/10.1007/s11630-998-0021-1>.
11. **Koch, L.D.; Bridges, J.** 2004. Mean flow and noise prediction for a separate flow jet with chevron mixers, 42nd Aerospace Sciences Meeting and Exhibit. Reno, Nevada.
12. **Koutmos, P.; McGuirk, J.J.** 1995. CFD predictions of lobed mixer performance, *Comput. Methods Appl. Mech. Engrg.* 122: 131-144.
[http://dx.doi.org/10.1016/0045-7825\(94\)00744-8](http://dx.doi.org/10.1016/0045-7825(94)00744-8).
13. **Georgiadis, N.J.; DeBonis, J.R.** 2006. Navier–Stokes analysis methods for turbulent jet flows with application to aircraft exhaust nozzles, *Progress in Aerospace Sciences* 42: 377-418.
<http://dx.doi.org/10.1016/j.paerosci.2006.12.001>.
14. **Salman, H.; Page, G.J.; McGuirk, J.J.** 2003. Prediction of lobed mixer vortical structures with a k- ϵ turbulence model, *AIAA Journal* 41(5): 878-887.
<http://dx.doi.org/10.2514/2.2023>.
15. **Nathan, J.C.; Parviz, M.; Hu, H.** 2005. Numerical Simulation of the Vortical Structures in a Lobed Jet Mixing Flow, 43rd AIAA Aerospace Sciences Meeting and Exhibit. Reno, Nevada.
16. **Menter F.** 1994. Two-equation eddy-viscosity turbulence models for engineering applications, *AIAA Journal* 32: 1598-1605.
<http://dx.doi.org/10.2514/3.12149>.
17. **Meslem, A.; El-Hassan, M.; Nastase I.** 2011. Analysis of jet entrainment mechanism in the transitional regime by time-resolved PIV, *Journal of Visualization* 14(1): 41-52.
<http://dx.doi.org/10.1007/s12650-010-0057-7>.

A. Meslem, A. Dia, C. Beghein, A. Ammar, I. Nastase, M. El Hassan

LAISVOS KRYŽMINĖS SROVĖS SKAITINIS IMITAVIMAS

R e z i u m ė

Skaitinio turbulentinės kryžminės purkštuko srovės imitavimo, naudojant šlyties įtempių perdavimo $k\omega$ modelį, rezultatai palyginti su matavimų rezultatais. Šlyties įtempių perdavimo modelis gali prognozuoti ašių komutacijos reiškinį. Pradiniai ribiniai sluoksniai yra mažesni už prognozuojamus, o turbulentinė kinetinė energija viršija prognozuojamą. Minimalus srauto išplatėjimas ir maksimalus susiaurėjimas yra didesni už prognozuotus, o potencialus šerdies ilgis, sukuriantis srovės maksimalaus greičio mažėjimo stabdymą, yra pervertintas. Tačiau buvo nustatytos patenkinamos srovės skerspjūvio ir turinio tekėjimo greičio prognozės ir tai leido patikimai prognozuoti „vidutinio srovės spindulio“ ir „vidutinio srovės greičio“ įvertinimą. Mes esame suinteresuoti kaitinimo, vėdinimo ir oro kondicionavimo difuzorių optimizavimu naudojant srovės įsiurbimo pasyviąją kontrolę. Mentinės perforuotos sienelės yra naujoviški difuzoriai, palyginti su dabar naudojamais. Gauti rezultatai rodo, kad šlyties įtempių perdavimo $k\omega$ modelis yra efektyvus įrankis neapskritiminių purkštukų konstrukcijos optimizavimui projektavimo metu.

A. Meslem, A. Dia, C. Beghein, A. Ammar, I. Nastase, M. El Hassan

NUMERICAL SIMULATION OF FREE CROSS-SHAPED JET

S u m m a r y

Numerical simulation of a turbulent cross-shaped orifice jet using the SST $k\omega$ model is compared with measurements. The SST $k\omega$ model is able to predict the axis-switching phenomenon. The initial boundary layers are lower than reference values and turbulent kinetic energy is over predicted. The flow expansion in the minor plane and flow contraction in the major plane are more pronounced and the potential core length is overestimated generating a delay on the streamwise maximum velocity decay. However, satisfactory predictions of the flow transverse area and volumetric flow rate are observed and lead to good predictions of “mean flow radius” and “mean flow velocity” evolutions. We are interested in optimizing HVAC diffusers using the passive control of the jet induction. The lobed perforated panel is an innovative diffuser among others. The obtained results show that the SST $k\omega$ model is an efficient tool for quickly optimizing non-circular orifice design.

Keywords: numerical simulation, free cross-shaped jet.

Received March 07, 2011

Accepted June 13, 2012